INTERNATIONAL JOURNAL FOR NUMERICAL METHODS IN FLUIDS
Int. J. Numer. Meth. Fluids 2001; **36**: 249–263 (DOI: 10.1002/fld.127)

Lung effect on the hemodynamics in pulmonary artery

S. F. Tsai[a], Tony W. H. Sheu[a,*,1] and T. M. Chang[b,2]

[a] *Department of Naval Architecture and Ocean Engineering, National Taiwan University, Taipei, Taiwan, Republic of China*
[b] *Buddhist Tzu-Chi General Hospital, Hualien, Taiwan, Republic of China*

SUMMARY

The present study investigates blood flow in a pulmonary artery. The aim is to gain a better understanding of offset value in vascular circulation through a two-dimensional analysis of the Navier–Stokes equations. In this study, the hemodynamics in a blood vessel with truncated outlets at which constant pressure is specified is examined. To simplify the analysis, the vessel walls are regarded as being rigid. In quadratic elements, the streamline upwind Petrov–Galerkin finite element model is employed to simulate the incompressible Newtonian blood flow. The adopted finite element model introduces artificial damping terms solely in the streamline direction. With these terms added to the formulation, the discrete system is enhanced while solution accuracy is maintained without deterioration due to numerical diffusion errors. Copyright © 2001 John Wiley & Sons, Ltd.

KEY WORDS: constant pressure; hemodynamics; offset value; pulmonary artery

1. INTRODUCTION

According to Kim *et al.* [1], 7/1000 new born babies suffer from congenital heart defects. Their abnormal vascular systems are unable to provide adequate blood, which can result in impairment of the lungs. The Fontan operation [2] is a surgical means of fixing this problem by routing the blood to the lungs. Three main classes of such by-pass operations exist that are often referred to. They are the atriopulmonary connection (APC), the cavopulmonary connection (CPC) and the bidirectional cavopulmonary anastomosis (BCPA). The post-operation hemodynamic and energetic differences, albeit small, play a crucial role in the failure or success of the operation for a long-term follow-up patient [3]. As a result, a detailed understanding of the hemodynamics in vascular circulation is needed.

* Correspondence to: Department of Naval Architecture and Ocean Engineering, National Taiwan University, 73 Chow-Shan Road, Taipei, Taiwan, Republic of China. Fax: + 886 2 23929885.
[1] E-mail: Tony.Sheu@cfd.na.ntu.edu.tw
[2] Fax: + 886 3 85660977.

Received February 2000
Revised April 2000

In this study, we consider a clinical operation known as the total cavopulmonary connection (TCPC). This operation is widely used for surgery on hearts that essentially have a single ventricular chamber [4,5]. As Figure 1 shows, the TCPC operation involves disconnection of the pulmonary artery from its ventricular origin and anastomosis of the superior vena cava (SVC) with the right pulmonary artery. The operation reconstructs a right atrial lateral tunnel so as to connect the inferior vena cava (IVC) to the transected end of the SVC, which is anastomosed to the right main pulmonary artery. This TCPC operation by-passes the right heart and creates circulation driven solely by a single ventricular pump. As the energy generated by the left ventricular pump is mostly dissipated in the systemic circulation, the hemodynamics in the venae cavae and the pulmonary circulation are particularly precarious. This motivated us to learn more about the hemodynamics in the anastomotic region.

Long-term success of a surgically created circuit requires avoiding blood reversal in the vascular circulation. This abnormality may induce low wall shear stress and oscillating shear stress in pulsatile situations. Both of them have been found to correlate with atherosclerotic plaque localization. Also, high shear stresses can damage the blood vessel. Another key aspect in the cardiac surgery is that surgically created monoventricular circulation should provide adequate pulmonary perfusion for the global circulatory system. In fluid dynamic terms, proper pressure and blood flow rates in the pulmonary arteries are of primary importance. Also, elevation of the post-operative central venous pressure should be avoided for an operation to be termed successful. Achieving these goals poses a grand challenge to cardiac surgeon doctors when they conduct TCPC surgical procedures.

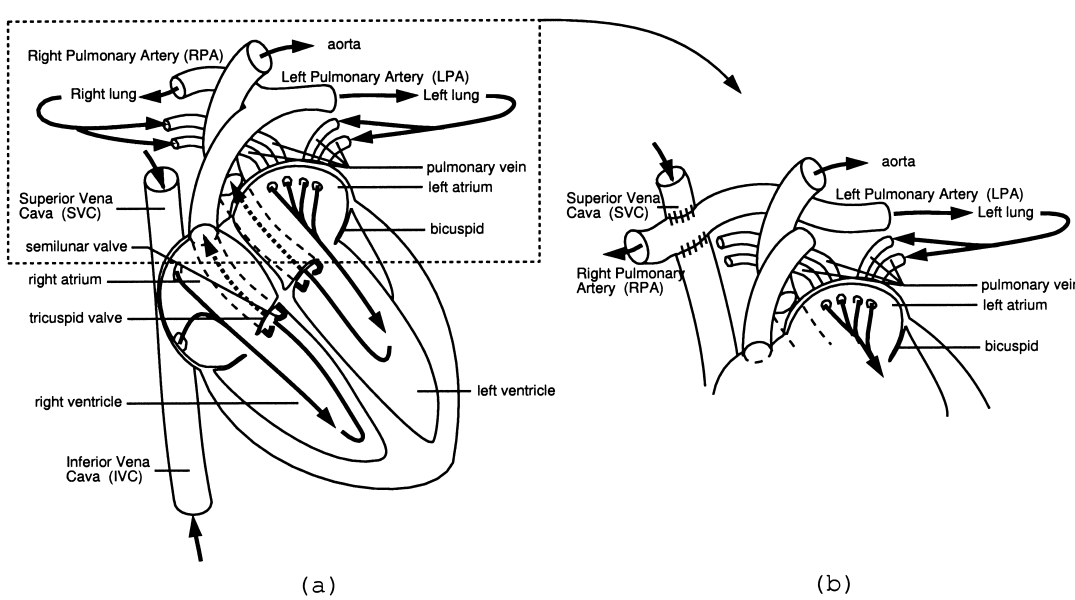

Figure 1. (a) Schematic drawing of anatomy of normal vascular circulation system; (b) illustration of anatomy after TCPC anastomosis.

In the past two decades extensive experimental efforts have been devoted to exploring vascular blood transport phenomena and significant contributions have been made to our understanding of vascular disease. Experimental success in conducting blood flow visualization has, however, been overshadowed by increasingly higher costs and time-consuming clinical procedures. Most serious is that it is still infeasible to use working fluids with the same characteristics as blood. In recent years, improvements in hardware and software have enabled investigators to use computational fluid dynamics techniques to investigate complex hemodynamics in greater detail [6]. Numerical simulation of hemodynamics by a finite element method has received increased attention because of its prevailing advantage in handling complex geometries. In the early days, efforts were made in two-dimensional studies [7–9]. Since the pioneering work of Wille [10], three-dimensional hemodynamic simulations have become increasingly feasible due to the increased computer speed by several orders of magnitude in the last decade. This breakthrough enabled Rindt and Perktold [11,12] to extend their carotid blood flow simulation into three dimensions. This article presents our recent research into the modeling of blood flow in the human vascular system.

The rest of this paper is organized as follows. In Section 2 we present Navier–Stokes equations that are written in terms of primitive variables. Equations of motion are solved subject to the constraint condition to ensure mass conservation. For the elliptic equations to be well-posed, boundary conditions are prescribed. Section 3 presents the weighted residuals statement for governing equations that are subject solely to the Dirichlet-type boundary conditions for both velocity and pressure. It is shown that the case with pressure prescribed *a priori* at the vessel exit can be theoretically modeled. This is followed by the introduction of the finite element used and application of the upwind model to resolve pressure and velocity oscillations respectively. In Section 4 we describe the test problem in greater detail. The results obtained from this hemodynamic study on blood flow in a TCPC vessel are presented in Section 5. Finally, we draw conclusions in Section 6.

2. MATHEMATICAL MODEL

Numerical modeling of blood flow requires solving three-dimensional flow equations in a distensible vessel. To facilitate vascular flow analysis in a deformable blood vessel, a much more sophisticated numerical model, such as the arbitrary Lagrangian–Eulerian (ALE) model [13,14], is needed. As a first approximation, the vessel wall is assumed to be rigid. The vessel diameter change per cardiac cycle is, usually, around 5–10 per cent in most of the major arteries. We consider this assumption rational since the global flow structure and the stress pattern remain unchanged [15]. To further simplify the analysis, two-dimensional working equations are considered.

In this study the vessel is considered to be symmetric about the midplane (x–y plane) and this plane is taken as the solution domain, shown schematically in Figure 2. According to surgical reports, it is legitimate to assume that the flow is laminar [16]. Another assumption we make is that the blood under investigation is a Newtonian fluid since in the major arteries the shear strain rate of the blood flow typically can be regarded as a constant value [17]. In addition, blood is a suspension of red blood cells, white blood cells, platelets and proteins,

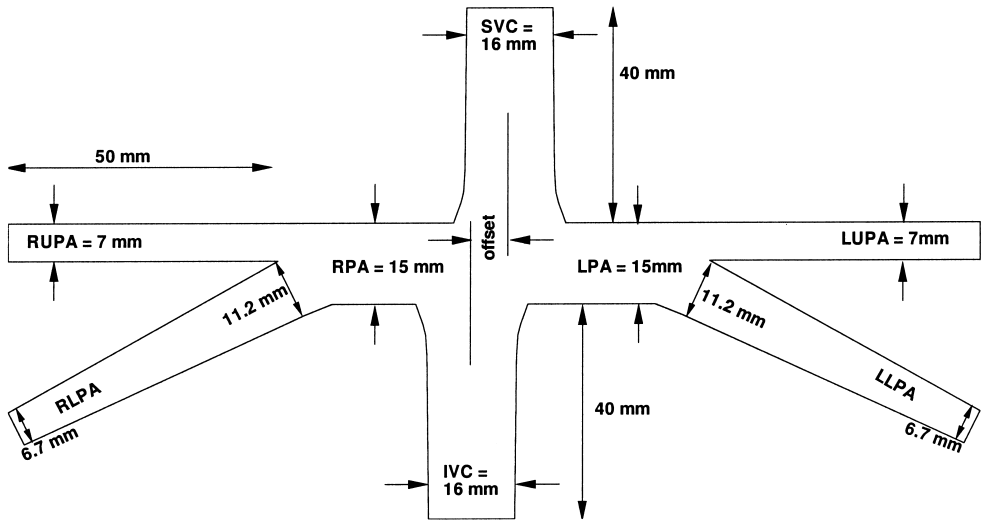

Figure 2. Schematic of the TCPC model and the definition of the offset value.

whose sizes are much smaller than the characteristic length of the artery. Therefore, blood can be treated as being homogeneous and incompressible. Under these circumstances, working equations adequate for a steady blood flow simulation in the vascular system, Ω, are made dimensionless as follows:

$$\underline{u}\cdot\nabla\underline{u} = -\nabla p + \frac{1}{Re}\nabla^2\underline{u} \tag{1}$$

$$\nabla\cdot\underline{u} = 0 \tag{2}$$

Based on the chosen reference length, L, and the characteristic velocity, U, the Reynolds number is expressed as $Re = Re = UL/v$, where v is the kinematic viscosity of the blood flow. The reason for advocating the primitive variable formulation is the accommodated closure boundary condition [18]. Since the differential system is classified as being elliptic, specification of boundary conditions along the entire boundary of the domain is required to close the differential system. In this paper, we will address how the pressure boundary condition can be applied at the truncated vessel exit.

3. NUMERICAL MODEL

In this study, we seek the steady state solutions of the Navier–Stokes and continuity equations using a method suited to solving complex geometry problems. To ensure that the velocity

vector accommodates the divergence-free property, we adopt the mixed formulation (see, e.g., Reference [19]). In the context of the weighted residuals finite element method, we denote by $\mathscr{L}^2(\Omega)$ the space of functions that are square integrable over Ω. We also define its constrained space $\mathscr{L}^2_0(\Omega)$ $(\equiv \{q \in \mathscr{L}^2(\Omega) = \int_\Omega q \, d\Omega = 0\})$, which consists of square integrable functions having zero mean over Ω. In the mixed finite element analysis of Navier–Stokes equations, we need to define the Sobolev space $\mathscr{H}^1(\Omega) = \{q \in \mathscr{L}^2(\Omega)\colon \mathscr{D}q \in \mathscr{L}^2(\Omega)\}$. Here, $\mathscr{D}$ denotes the derivative of order 1. In addition, the subspace of $\mathscr{H}^1(\Omega)$, namely $\mathscr{H}^1_0(\Omega)$, is introduced to close the weighted residuals statement. By definition, all the elements in $\mathscr{H}^1_0(\Omega)$ have one square integrable derivative over Ω and vanish on the boundary Γ: $\mathscr{H}^1_0(\Omega) = \{q \in \mathscr{H}^1(\Omega)\colon\ q = 0 \ \text{ on } \ \Gamma\}$.

Having defined the above functional spaces, we can present the weighted residuals statement as follows: given an admissive function $\underline{w} \in \mathscr{H}^1_0(\Omega) \times \mathscr{H}^1_0(\Omega) \equiv \mathbf{H}^1_0$ and a pressure mode $q \in \mathscr{L}^2_0(\Omega) = \mathscr{P}$, find solutions of $(\underline{u}, p) \in V \equiv \mathbf{H}^1_0 \times \mathscr{P}$ from the following equations:

$$\int_\Omega (\underline{u} \cdot \nabla)\underline{u} \cdot \underline{w} \, d\Omega + \frac{1}{Re} \int_\Omega \nabla \underline{u} \colon \nabla \underline{w} \, d\Omega - \int_\Omega p \nabla \cdot \underline{w} \, d\Omega = \int_{\Gamma/\Gamma_n} r\underline{w} \cdot \underline{n} \, d\Gamma + \int_{\Gamma/\Gamma_r} \underline{s} \cdot \underline{w} \times \underline{n} \, d\Gamma \tag{3}$$

$$\int_\Omega (\nabla \cdot \underline{u}) q \, d\Omega = 0 \tag{4}$$

where

$$-p + \frac{1}{Re} \underline{n} \cdot \nabla \underline{u} \cdot \underline{n} = r \quad \text{ on } \ \Gamma/\Gamma_n \tag{5}$$

$$\frac{1}{Re} \underline{n} \cdot \nabla \underline{u} \times \underline{n} = \underline{s} \quad \text{ on } \ \Gamma/\Gamma_r \tag{6}$$

To specify a boundary condition on Γ, we denote two boundary segments as Γ_n and Γ_r. Note that Γ/Γ_i $(i = n, r)$ shown in Equations (5) and (6) are defined as the complement of Γ_i in Γ in the sense that if a vector $\underline{\phi}$ belongs to Γ/Γ_i, then $\underline{\phi} \in \Gamma$ but $\underline{\phi} \notin \Gamma_i$. In the above, $\underline{w} \in \mathscr{H}^1_0(\Omega) \times \mathscr{H}^1_0(\Omega)$ and $q \in \mathscr{L}^2_0(\Omega)$ are the test functions for the vector and scalar quantities respectively. In Equation (6), vector $\underline{s}$ denotes the unit tangent to Γ.

In the finite element analysis of Equations (3)–(6), we can approximate $\underline{u}$ by means of $\underline{u}^h = \Sigma\, u^h_i N^h_i$ and $p^h = \Sigma\, p^h_i M^h_i$, where $\{N^h_i\}$ and $\{M^h_i\}$ are the basis functions for the vector $\underline{u}$ and the scalar p respectively. These basis functions are chosen to be able to satisfy the inf–sup condition and thus avoid node-to-node pressure oscillations [20,21]. To this end, we employ biquadratic polynomials, N_i $(i = 1 \sim 9)$, to approximate $\underline{u}$ and use bilinear polynomials, M_i $(i = 1 \sim 4)$, to approximate p. This variable setting resembles the staggered meshes used in the finite volume methods to store the pressure and velocity unknowns.

The assembled matrix equations for a problem having n^e elements take the form $\underline{\underline{A}}\,\underline{q} = \underline{b}$ for the solution vector $\underline{q} = (u_j, v_j, p_j)^T$. The matrix $\underline{\underline{A}}$ is derived as

$$a_{ij} = \sum_{1}^{n^e} \int_{\Omega^h} \begin{pmatrix} C^{ij} & 0 & -M^j \dfrac{\partial N^i}{\partial x_1} + B^i \dfrac{\partial M^i}{\partial x_1} \\ 0 & C^{ij} & -M^j \dfrac{\partial N^i}{\partial x_2} + B^i \dfrac{\partial M^i}{\partial x_2} \\ M^i \dfrac{\partial N^j}{\partial x_1} & M^i \dfrac{\partial N^j}{\partial x_2} & 0 \end{pmatrix} \mathrm{d}\Omega^h$$

$$+ \int_{\Gamma^h} \begin{pmatrix} -\dfrac{1}{Re} N^i \dfrac{\partial N^j}{\partial x_k} \cdot n_k & 0 & 0 \\ 0 & -\dfrac{1}{Re} N^i \dfrac{\partial N^j}{\partial x_k} \cdot n_k & 0 \\ 0 & 0 & 0 \end{pmatrix} \mathrm{d}\Gamma^h \tag{7}$$

In Equation (7), C^{ij} accounts for equation non-linearity and is expressed as

$$C^{ij} = (N^i + B^i) N^j \tilde{V}_k^j \frac{\partial N^j}{\partial x_k} + \frac{1}{Re} \frac{\partial N^i}{\partial x_k} \frac{\partial N^j}{\partial x_k} - \frac{1}{Re} B^i \frac{\partial^2 N^j}{\partial x_k \, \partial x_k} \tag{8}$$

In finite element analysis of Navier–Stokes equations, $\tilde{U}$ and $\tilde{V}$ are assumed to be constant when evaluating the matrices. The line integral shown in Equation (7) represents the contribution of the essential-type boundary conditions. At boundaries where natural boundary conditions are imposed, the vector $\underline{b}$ is given by

$$\underline{b} = \int_{\Gamma^h} \begin{pmatrix} -N^i p_i n_1 \\ -N^i p_i n_2 \\ 0 \end{pmatrix} \mathrm{d}\Gamma^h \tag{9}$$

Here (n_1, n_2) denotes the outward vector normal to the boundary, at which pressure values are imposed. It is the above equation that clearly explains why pressure values are admitted to be specified at the boundary.

In numerical simulation of blood flows, proper selection of the test space $\underline{w}$ is vital to suppressing velocity oscillations. To enhance the convective stability, we consider the Petrov–Galerkin finite element model. This model is regarded as a modification of the Galerkin method in the sense that the biased polynomial

$$B^i = \tau N^j \tilde{V}_k^j \frac{\partial N^i}{\partial x_k} \tag{10}$$

is added to the basis function N^j. As a result of adding B_i to Equation (8), field variables on the upwind side are favorably considered. The free parameter τ shown in Equation (10) determines the upwinding needed to suppress oscillatory velocities. In the above equation, $\tilde{V}$

stands for velocities that are evaluated at element centroids. In our Petrov–Galerkin model, we consider τ ($\equiv \delta(\gamma)/2|\underline{u}|^2$) as a function of the Peclet number, $\gamma = |\underline{u}|h/2\mu$. Specific to our finite element analysis is that δ has been analytically derived from the one-dimensional convection–diffusion scalar transport equation in quadratic elements. Depending on the nodal classification, the following expressions of δ have been analytically obtained and computationally validated in quadratic elements [22]

$$\delta(\gamma) = \begin{cases} \dfrac{1}{2}\coth\left(\dfrac{\gamma}{2}\right) - \dfrac{1}{\gamma}; & \text{center node} \\ \dfrac{\gamma \sinh\gamma\cosh\gamma - \sinh^2\gamma - 4\cosh\gamma - 2\gamma\sinh\gamma - 4}{6\sinh\gamma\cosh\gamma + \gamma\sinh^2\gamma - 6\sinh\gamma - 4\gamma\cosh\gamma + 4\gamma}; & \text{corner nodes} \end{cases} \tag{11}$$

Before entering into a discussion of the results, it is important to adopt the present fully-weighted upwind model. While the algebraical manipulation on diffusive terms is considerable, the fully-weighted model can enhance the discrete system, in particular in cases when the grid size has a marked change. Readers are referred to Reference [22] for additional details. Another noteworthy feature is that use of the streamline operator given in Equation (10) makes it possible to add the artificial viscosity $|\underline{u}^2|\tau\phi_{ss}$ to the primary flow direction. This artificial damping term is considered useful not only for stabilizing the system, but also for decreasing the numerical diffusion errors in the multi-dimensional flow analysis [22].

4. PROBLEM DESCRIPTION

As the anatomy shown in Figure 2 reveals, blood from the the SVC and IVC are confluent, followed by a downstream flow into the left pulmonary artery (LPA) and right pulmonary artery (RPA). Further downstream, the main pulmonary artery bifurcates into four branches: the left upper pulmonary artery (LUPA), left lower pulmonary artery (LLPA), right upper pulmonary artery (RUPA) and right lower pulmonary artery (RLPA). These branch flows proceed further downstream to the left and right lungs. According to angiocardiograms, the vessel diameters investigated were 16 mm for the SVC and the IVC, 7 mm for the LUPA and RUPA and 6.7 mm for the RLPA and LLPA respectively. The diameter of both the RPA and LPA was 15 mm. To obtain a better flow distribution and energy dissipation, it is useful to enlarge the IVC and SVC anastomoses. Therefore, the diameters of the SVC and IVC increased gradually to 130 per cent diameter enlargement at the IVC and SVC anastomoses near the main pulmonary.

As clinical reports indicate, the blood in the SVC carries approximately one-third of the systemic venous return and goes preferentially to the larger right lung. As for the blood in the IVC, it carries the rest of the systemic venous return and goes to the smaller left lung. To simplify the analysis, the velocity boundary condition specified at the inlets of the SVC and IVC had a non-pulsatile steady parabolic profile. The flow rates were kept constant: $Q_{IVC} = 2.4\ \mathrm{l\,min^{-1}}$ and $Q_{SVC} = 1.2\ \mathrm{l\,min^{-1}}$. Therefore, the maximum inlet velocities of the IVC and SVC were obtained as 0.3 and 0.15 $\mathrm{m\,s^{-1}}$ respectively. According to the density, $\rho = 1060$

kg m^{-3}, and the Newtonian blood viscosity, $\mu = 3 \times 10^{-3}$ Pa s, the Reynolds number under investigation was 565. This value was obtained by choosing $D = 0.016$ m as the reference length and $\bar{u} = 0.1$ m s^{-1} as the characteristic velocity.

To close the investigated elliptic-type differential system, there remains the specification of outlet boundary conditions. Since lungs tend to impose a resistance force on the blood flow in the LUPA, LLPA, RUPA and RLPA, it is important to take into account the effect of the lung on the hemodynamic simulation. To this end, we adopt the lumped-parameter pulmonary circulation model [23] to close the Navier–Stokes flow simulation. Provided that the pulmonary resistance, R_{lung}, and left atrium pressure, p_{LA}, are available in the cardiac catheterization report, the pressure prescribed at the truncated vessel outlet can be determined using the underlying lumped-parameter model

$$p_i = p_{\text{LA}} + R_{\text{lung}} Q_i \quad (i = \text{LUPA, RUPA, RLPA, LLPA}) \tag{12}$$

In this study p_{LA} was chosen to be 400 Pa and R_{lung} as 25.9 Pa cm^{-3} s.

5. RESULTS AND DISCUSSION

The physical domain under investigation is schematically shown in Figure 2. Five offset values, OFS = 7, 5, 0, -4 and -6 mm, are considered. These offset values have been investigated in our previous study [24]. To resolve the flow detail, grids were clustered near the vessel wall and in regions where the vessel configuration underwent a marked change (Figure 3). As the geometrical complexity makes scheme-convergence difficult, it is important to assure that the computed finite element results are indeed the convergent solutions. For this purpose, we

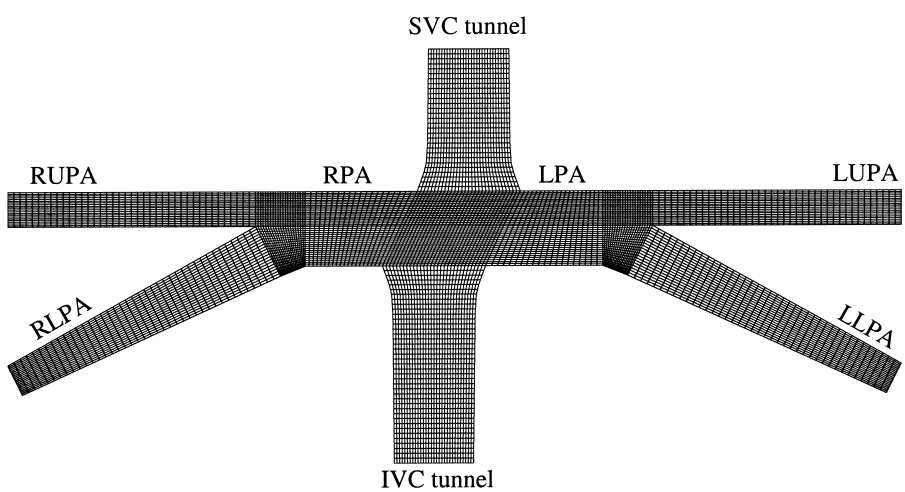

Figure 3. Finite element mesh points for the hemodynamic analysis in the TCPC model.

plotted the convergence histories for all the primitive variables against iteration numbers. For this study $|\underline{u}|^{k+1} - |\underline{u}|^k$ and $p^{k+1} - p^k$ were cast in their L_2-norm forms, where the superscripts k and $k+1$ are two consecutive iteration numbers. Take the case with the offset value of 7 mm as an example, the fast convergence shown in Figure 4 reveals the applicability of the biquadratic finite element code to modeling blood flow in vascular circulation.

Due to space limitation, we plot results mainly for the case of OFS = 7 mm. Figure 5 plots the streamline contours, where a topological saddle point is seen in the junction region. Blood in the SVC flows mostly to the LPA, which results in the left SVC vessel being the pressure side and the inner wall the suction side (Figure 6). On the other hand, the pressure side of the IVC vessel is on the reader's left-hand side while the suction side of the IVC vessel is regarded as being the suction side. To provide readers insight into the flow development in the pulmonary artery, we plotted velocity profiles at some selected sections. Figure 7 provides another picture of the blood division in the juncture region.

As the left and right lungs are different in size, the distribution of blood volume is a crucial factor in TCPC operations. Therefore, we had to know how blood flows from SVC and IVC distributed to the RPA and UPA. To this end, we plot dividing lines for five investigated offset values in Figure 8. We proceeded to integrate the computed velocities on four outlet planes. The resulting blood volumes are plotted in Figure 9 against the offset values. This plot helps obtain the volumetric flow ratio QR [$\equiv (Q_{\mathrm{LUPA}} + Q_{\mathrm{LLPA}})/(Q_{\mathrm{RUPA}} + Q_{\mathrm{RLPA}})$] and we plot them in Figure 10.

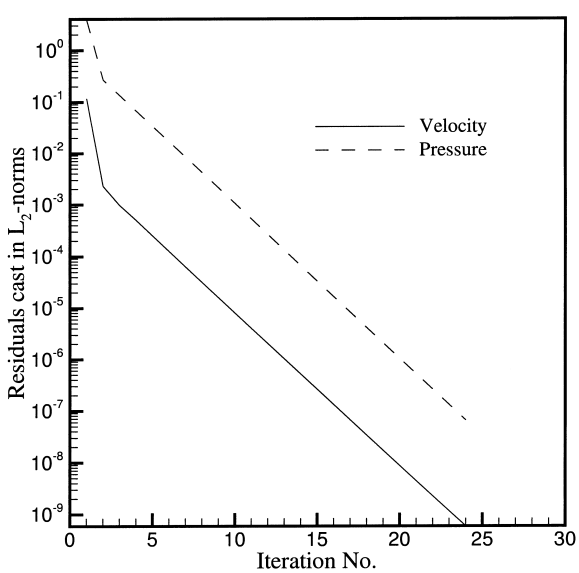

Figure 4. Histories of convergence for $|\underline{u}|$ and p.

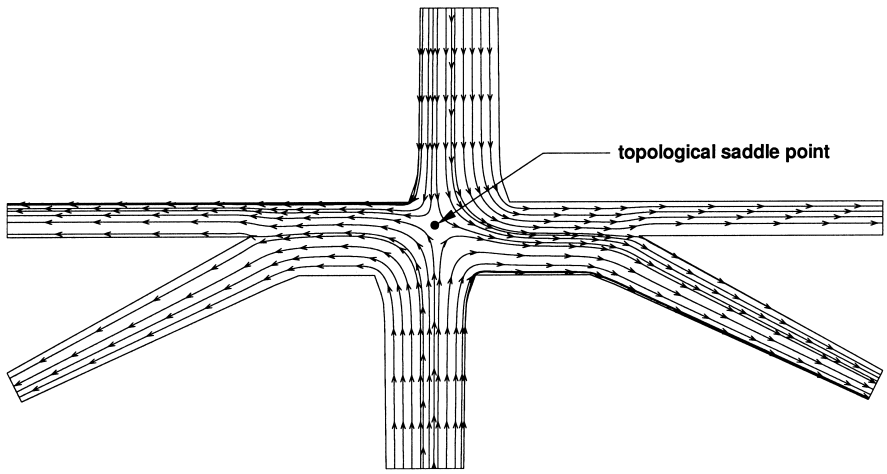

Figure 5. Predicted streamline contours for the case with the offset value of 7 mm.

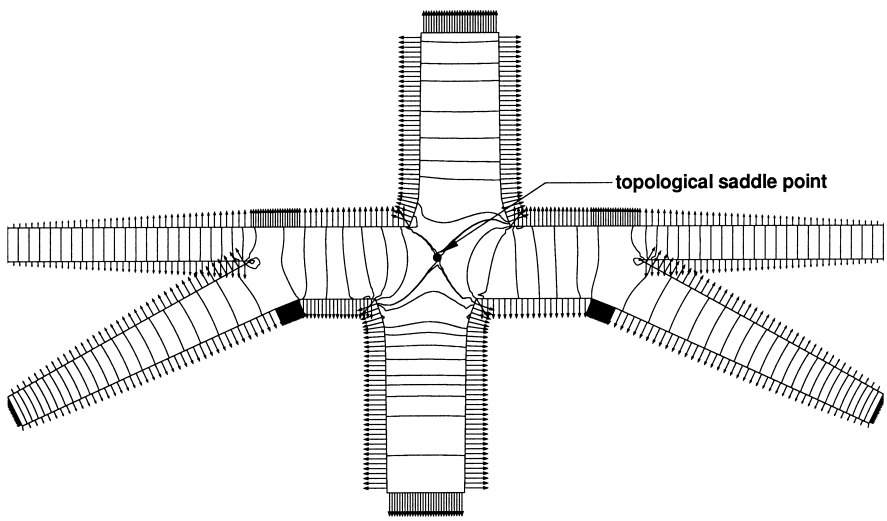

Figure 6. Pressure contours and pressure distributions along the vessel wall.

It has been known for quite some time that a marked change in configuration inevitably results in an energy loss. As a result, a better design for connections in TCPC surgical operations involves measuring some energetic indices. Two important parameters are often referred to. The first one is the total energy loss coefficient C_e, defined as follows:

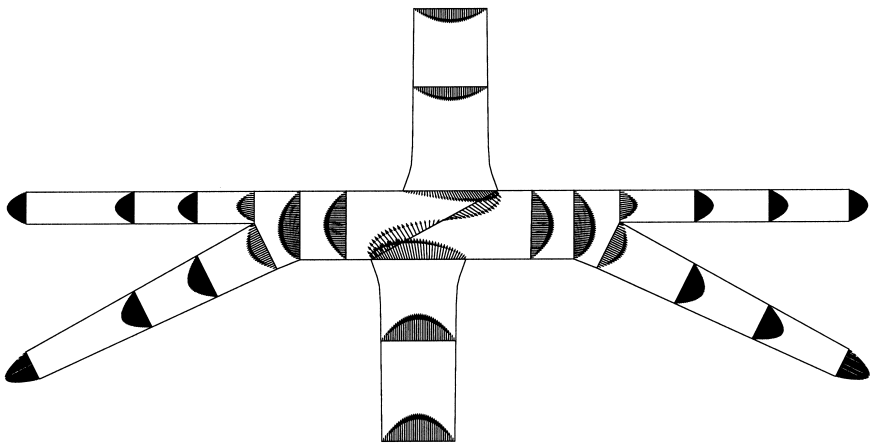

Figure 7. Velocity vector plots for the case with offset value 7 mm.

$$C_e = \frac{(\frac{1}{2}\rho V_{IVC}^2 + P_{IVC})Q_{IVC} + (\frac{1}{2}\rho V_{SVC}^2 + P_{SVC})Q_{SVC} - \sum_i (\frac{1}{2}\rho V_i^2 + P_i)Q_i}{\frac{1}{2}\rho(V_{IVC}^2 Q_{IVC} + V_{SVC}^2 Q_{SVC})},$$
$$i = \text{LUPA, LLPA, RUPA, RLPA} \tag{13}$$

The other indicator of primary importance is the hydraulic power given below

$$\dot{W}_d = \left(\frac{1}{2}\rho V_{IVC}^2 + P_{IVC}\right)Q_{IVC} + \left(\frac{1}{2}\rho V_{SVC}^2 + P_{SVC}\right)Q_{SVC} - \sum_i \left(\frac{1}{2} V_i^2 + P_i\right)Q_i,$$
$$i = \text{LUPA, LLPA, RUPA, RLPA} \tag{14}$$

The computed values of C_e and $\dot{W}_d$ for five investigated offset values are shown graphically. As Figure 11 illustrates, the best offset value is chosen to be 7 mm of the five investigated cases.

6. CONCLUSIONS

This paper has described a numerical simulation of blood flow to the lungs after a Fontan surgical procedure was conducted. The emphasis of this study is to take the lung resistance into consideration in the present hemodynamic analysis. Depending on the blood volume, the pressure prescribed at the four exits of the pulmonary arteries are implemented in the mixed finite element code with a sound theoretical foundation. Through this TCPC hemodynamic

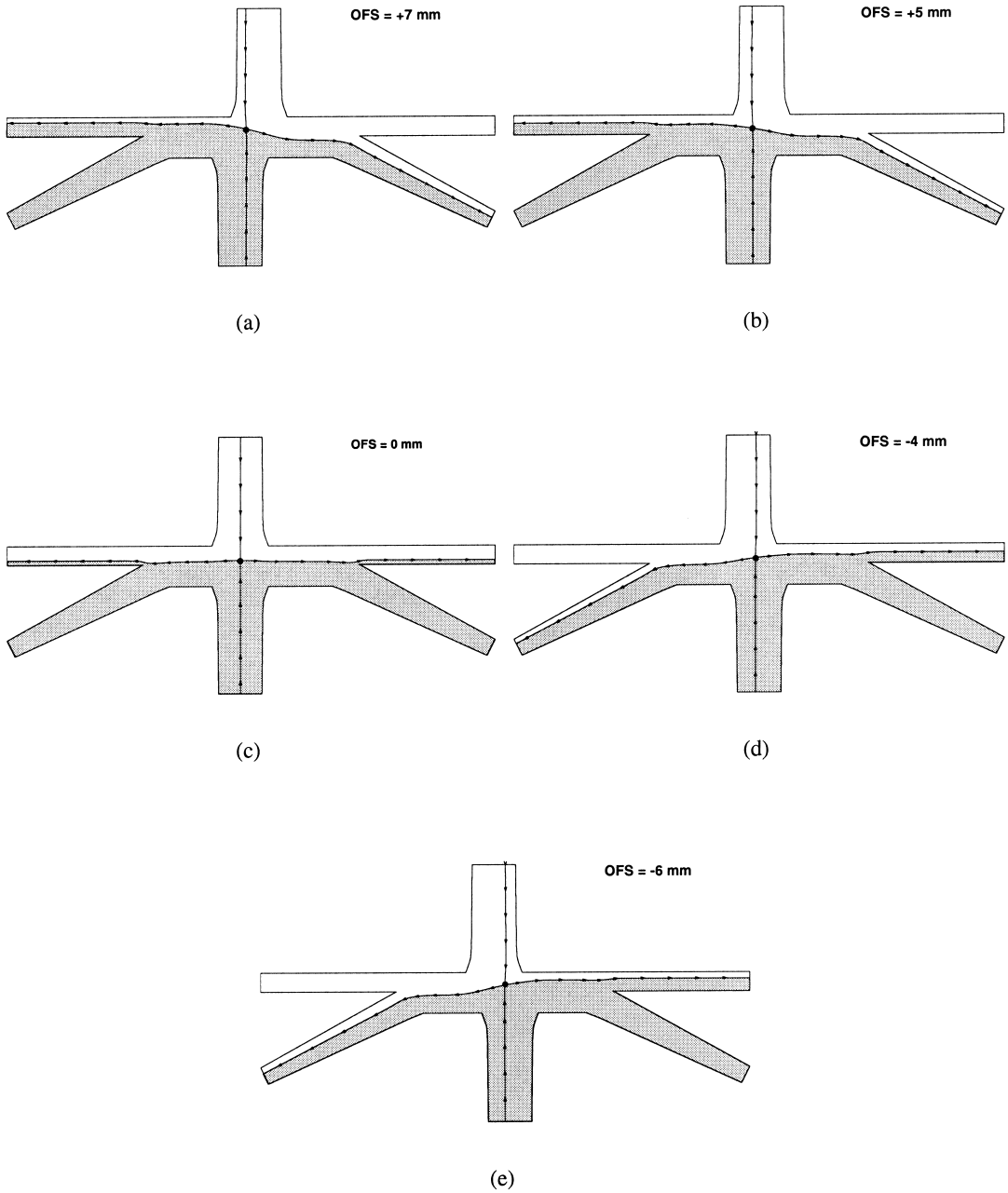

Figure 8. Blood dividing lines from IVC and SVC to the LPA and RPA for five investigated offset values: (a) 7 mm; (b) 5 mm; (c) 0 mm; (d) -4 mm; (e) -6 mm. '●' denotes the topological saddle point. The shaded area is the blood from IVC.

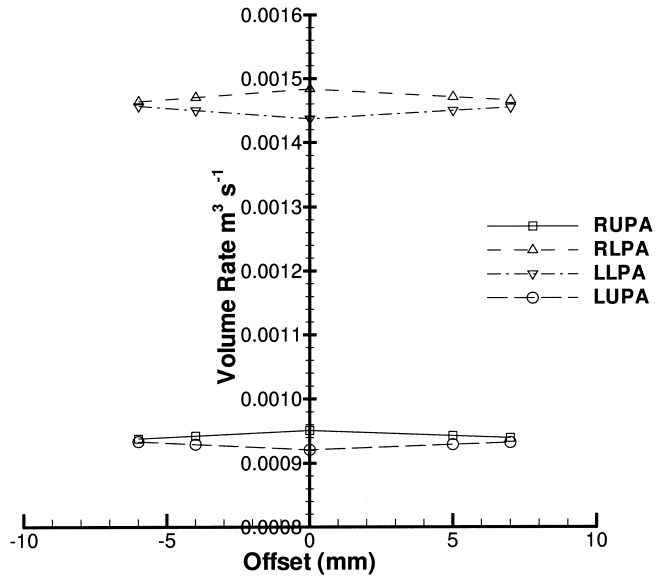

Figure 9. Computed blood volumes at four exit planes against offset values.

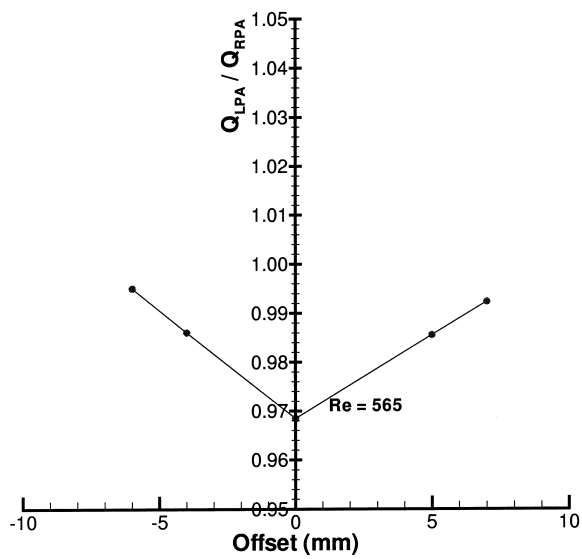

Figure 10. Computed LPA and RPA blood volume ratios against offset values.

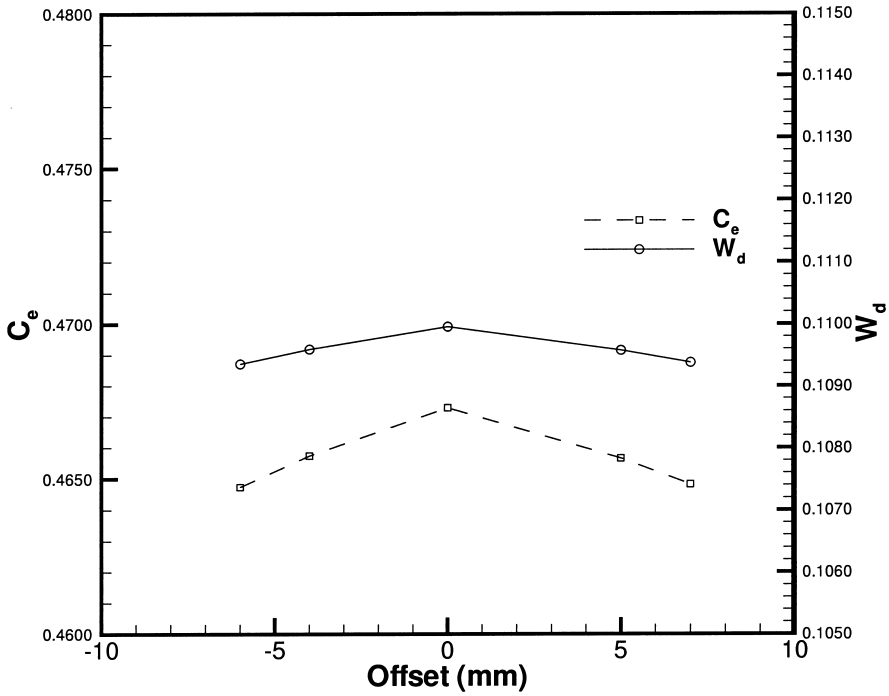

Figure 11. Computed C_e and W_d for five investigated offset values.

study, a clear flow structure has been revealed and helps us to determine the appropriate offset value for the blood distribution in the left and right pulmonary arteries.

ACKNOWLEDGMENTS

The authors would like to thank I.S. Chiu, the clinical professor of surgery of the medical college congenital cardiac surgeon of the National Taiwan University Hospital, who provided useful information in the course of this study. Research support provided by the National Science Council under Grant NSC 87-2213-E-002-002 is also gratefully acknowledged.

REFERENCES

1. Kim YH, Walker PG, Fontaine AA, Panchal S, Ensley AE, Oshinski J, Sharma S, Ha B, Lucas CL, Yoganathan AP. Hemodynamics of the Fontan connection: an in vitro study. *ASME*, *Journal of Biomechanical Engineering* 1995; **117**: 423–428.
2. Fontan F, Baudet E. Surgical repair of tricuspid atresia. *Thoracic* 1971; **26**: 240–248.
3. Fontan F, Kirklin JW, Fernandez G, Costa F, Naftel DC, Tritto F, Blackstone EH. Outcome after a perfect Fontan operation. *Circulation* 1990; **81**: 1520–1536.
4. de Leval MR, Kilner P, Gewiling M, Bull C. Total cavopulmonary connection: a logical alternative to atripulmonary connection for complex Fontan operation. *Journal of Thoracic Cardiovascular Surgery* 1988; **96**(5): 682–695.

5. Dubini G, de Leval MR, Pietrabissa R, Montevecchi FM, Fumero R. A numerical fluid mechanical study of repaired congenital heart defects application to the total cavopulmonary connection. *Journal of Biomechanics* 1996; **29**(1): 111–121.
6. Taylor C, Hughes TJR, Zarins C. Computational investigations in vascular disease. *Computers in Physics* 1996; **10**(3): 224–232.
7. Perktold K, Hilbert D. Numerical simulation of pulsatile flow in a carotid bifurcation model. *Journal of Biomedical Engineering* 1986; **8**: 193–198.
8. Rindt CCM, Van De Vosse FN, Van Steenhoven AA, Janssen JD, Reneman RS. A numerical and experimental analysis of the flow field in a two-dimensional model of the human carotid artery bifurcation. *Journal of Biomechanics* 1987; **20**: 499–509.
9. Patil MK, Subbaraj K. Finite element analysis of two dimensional steady flow in model arterial bifurcation. *Journal of Biomechanics* 1988; **21**: 219–233.
10. Wille SO. Numerical simulations of steady flow inside a three dimensional aortic bifurcation. *Journal of Biomedical Engineering* 1984; **6**: 49–55.
11. Rindt CCM, Van Steenhoven AA, Janssen JD, Reneman RS, Segal A. A numerical analysis of steady flow in a three-dimensional model of the carotid bifurcation. *Journal of Biomechanics* 1990; **23**: 461–473.
12. Perktold K, Resch M. Numerical flow studies in human carotid artery bifurcation: basic discussion of the geometric factor in atherogenesis. *Journal of Biomedical Engineering* 1990; **12**: 111–123.
13. Hirt CW, Amsden AA, Cook JC. An arbitrary Lagrangian–Eulerian computing method for all flow speeds. *Journal of Computational Physics* 1974; **14**: 227–253.
14. Hughes TJR, Liu WK, Zimmermann TK. Lagrangian–Eulerian finite element formulation for incompressible viscous flows. *Computer Methods in Applied Mechanics and Engineering* 1981; **29**: 329–349.
15. Perktold K, Rappitsch G. Computer simulation of local blood flow and vessel mechanics in a compliant carotid artery bifurcation model. *Journal of Biomechanics* 1995; **28**(7): 845–856.
16. Nerem RM. Vascular fluid mechanics, the arterial wall, and atherosclerosis. *Journal of Biomechanical Engineering* 1992; **114**: 274–282.
17. Fung YC. *Biomechanics: Motion, Flow Stress, and Growth*. Springer: New York, 1990.
18. Quartapelle L. *Numerical Solution of the Incompressible Navier–Stokes Equations*. Birkhäuser: Berlin, 1993.
19. Quarteroni A, Valli A. *Numerical Approximation of Partial Differential Equations*. Springer: Berlin, 1994.
20. Brezzi F, Douglas J. Stabilized mixed methods for the Stokes problem. *Numerische Mathematika* 1988; **53**: 225–235.
21. Babuška I. Error bounds for finite element methods. *Numerische Mathematika* 1971; **16**: 322–333.
22. Sheu TWH, Tsai SF, Wang MMT. Discussion of numerical deficiency of applying a partially-weighted upwind finite element model to incompressible Navier–Stokes equations. *Numerical Heat Transfer, Part B: Fundamentals* 1997; **32**: 197–214.
23. de Leval MR, Dubini G, Migliavacca F, Jalali H, Camporini G, Redington A, Pietrabissa R. Surgery for congenital heart disease. *Journal of Thoracic and Cardiovascular Surgey* 1996; **111**(3): 502–513.
24. Sheu TWH, Tsai SF, Hwang WS, Chang TM. A finite element study of the blood flow in total cavopulmonary connection. *Computer and Fluids* 1999; **28**(1): 19–39.

